

Signatures of particle diffusion in the x-ray spectrum of the blazar Mkn 421C. Baheeraja,^{1,*} S. Sahayanathan,^{2,3,†} F. M. Rieger,^{4,5,‡} and C. D. Ravikumar^{1,§}¹*Department of Physics, University of Calicut, Malappuram, Kerala, India*²*Astrophysical Sciences Division, Bhabha Atomic Research Centre, Mumbai—400085, India*³*Homi Bhabha National Institute, Mumbai 400094, India*⁴*Max Planck Institute for Plasma Physics (IPP), Boltzmannstraße 2, 85748 Garching, Germany*⁵*Institute for Theoretical Physics, Heidelberg University, Philosophenweg 12, 69120 Heidelberg, Germany*

(Received 14 December 2023; accepted 17 April 2024; published 24 May 2024)

The curvature in the blazar spectrum has the potential to understand the particle dynamics in jets. We performed a detailed analysis of simultaneous *Swift*-XRT (0.3–10 keV) and *NuSTAR* (3–79 keV) observations of Mkn 421. Our analysis of *NuSTAR* observations alone reveals that, during periods of low flux, the hard x-ray spectra are best represented by a steep power-law with photon index reaching ~ 3 . However, the spectrum exhibits significant curvature during its high flux states. To investigate this, we explore plausible diffusion processes facilitating shock acceleration in the emission region that can contribute to the observed spectral curvature. Particularly, such processes can cause gradual fall of the photon spectrum at high energies which can be represented by a subexponential function. The parameter that decides this spectral change can be used to characterize the energy dependence of the diffusive process. Our results suggest that the x-ray spectra of Mkn 421 are consistent with a scenario where particle acceleration is mediated through Bohm-type diffusion and the spectra beyond the synchrotron peak is modulated by the radiative loss process.

DOI: [10.1103/PhysRevD.109.103039](https://doi.org/10.1103/PhysRevD.109.103039)**I. INTRODUCTION**

Blazars are a class of active galactic nuclei (AGNs) with a relativistic jet closely aligned to the observer's line of sight [1,2]. They exhibit rapid flux variations at different timescales, spanning from minutes to years, across the entire electromagnetic spectrum [3]. These highly variable sources are characterized by two prominent peaks in their spectral energy distribution (SED), extending from radio to γ -ray energies. The low-energy SED component (peaking at the IR to x-ray regime) is commonly attributed to synchrotron emission by relativistic electrons [2,4]. On the other hand, the physical process responsible for the emission of the high-energy SED component (peaking at the MeV to TeV gamma-ray regime) is still under debate [e.g., 5, for a review].

Modeling the broadband synchrotron spectral component of blazars often suggests the emitting electron distribution to be a broken power-law [6–8]. In principle, a power-law electron distribution could be produced by Fermi-type particle acceleration [e.g., 9,10], where particles gain energy as they are scattered by magnetic turbulence

structures embedded in the jet. When electrons are scattered by the turbulent structures across a shock front, Fermi acceleration will be efficient and is commonly referred to as shock acceleration [e.g., 11,12]. Synchrotron cooling of a power-law electron distribution then results in a broken power-law distribution with power-law indices differing by one. The corresponding synchrotron photon spectrum would follow a broken power-law with indices differing by half [13,14]. However, broadband SED modeling of blazars often fails to support such an interpretation [e.g., 15]. In particular, our earlier study of the blazar Mkn 421 reported a strong anticorrelation between the spectral indices measured at lower and higher energies around the synchrotron spectral peak, disfavoring a simple radiative loss origin [16].

Narrow-band spectral analysis of blazars frequently reveals significant curvature around the peak of the synchrotron component, that is formally well represented by a log-parabola function [17–20]. However, such a function fails to explain the combined optical-UV and x-ray spectrum [18,21–23]. Instead, a smooth broken power-law or a power-law particle distribution with an exponential cutoff is often capable of explaining this broad-band spectral component [11,24]. Recent studies with high-resolution observations have revealed significant spectral curvature even beyond the synchrotron peak [22,25,26].

*baheeraja314@gmail.com

†sunder@barc.gov.in

‡frank.rieger@ipp.mpg.de

§cdr@uoc.ac.in

A simple description of first-order Fermi acceleration at shocks, assuming an energy-independent acceleration and escape time scale, naturally produces a power-law electron distribution. However, when radiative losses are taken into account and an energy-dependence is incorporated into the acceleration and/or escape time scales, the resulting particle distribution can deviate from a power-law and exhibit curvature toward high energies [11]. Similarly, a log-parabolic photon spectrum suggests the underlying electron distribution to be log-parabolic, which could be interpreted in terms of a statistical acceleration scenario with an energy-dependent acceleration probability [18]. In fact, under specific conditions, the electron distribution resulting from a stochastic particle acceleration could mimic a log-parabola [27]. It is then expected that the synchrotron peak energy anticorrelates with spectral curvature [28]. During the period of 1997–2006, an anticorrelation between the synchrotron peak energy and the spectral curvature was indeed found through log-parabolic spectral fitting of the x-ray data from Mkn 421 and other TeV BL Lacs, seemingly supportive of a stochastic acceleration scenario [21,27–29]. However, recent studies using *Swift*–*XRT*/*NuSTAR* observations report no significant correlation between these quantities [16,22,30–32]. On the other hand, a curved spectrum could also be the outcome of an energy-dependent escape from the acceleration region. When this energy-dependence is mild, the resulting electron distribution closely follows a log-parabolic shape [23] but deviates significantly otherwise. Synchrotron emission by an electron distribution originating in a model with a strong energy-dependent escape time scale has been used to fit the spectra of Mkn 421 during different flux states [33,34]. A strong correlation was observed between flux and the energy-dependence of the escape timescale, and this supports that Bohm type diffusion is prominent during high flux states.

Particle acceleration at non- or mildly relativistic shock fronts has for long been considered as one of the preferred mechanisms for generating the non-thermal particle distributions seen in AGN jets [e.g., 11,12,35–38]. The highest energy achieved by the accelerated particles, as well as the shape of the spectrum around the maximum energy, are influenced by the balance between acceleration, escape and the radiative energy loss rates. In the presence of synchrotron losses, shock acceleration (for example) can result in a power-law particle distribution with a modified exponential cutoff, $\propto \exp[-(\gamma/\gamma_c)^{\beta_e}]$, where β_e is dependent on the underlying turbulence/diffusion properties [e.g., 39]. Formally, $\beta_e = (1 + a)$ is related to the momentum index a of the spatial diffusion coefficient, $\kappa = (1/3)\lambda c \propto \gamma^a$, that facilitates the particle transport. Here, λ is the particle mean free path and γ is the particle Lorentz factor. In particular, one may have $\beta_e = 1$

($a = 0$) in the case of “idealized” hard-sphere scattering (energy-independent diffusion), $\beta_e = 4/3$ ($a = 1/3$) for Kolmogorov-type turbulence, and $\beta_e = 2$ ($a = 1$) for Bohm type diffusion (where $\lambda \sim r_g$, with r_g as the gyro-radius). Since the corresponding particle acceleration timescale, t_{acc} is proportional to λ , Bohm diffusion typically yields the fastest acceleration rate (i.e., the highest $\gamma_{e,\text{max}}$ when balanced with synchrotron losses). The resultant synchrotron spectra can exhibit some extended curvature at high energies. In particular, an electron distribution with exponential cutoff index β_e will result in a synchrotron spectrum which can be significantly smoother (subexponential) $j_\nu \propto \exp[-(\nu/\nu_c)^\zeta]$ with $\zeta \equiv \frac{\beta_e}{\beta_e + 2}$, e.g., $\zeta = 1/2$ in the case of Bohm-type diffusion [40].

The BL Lac object Mkn 421, that we focus on here, is the nearest ($z = 0.031$) and one of the well-studied TeV blazars. Mkn 421 belongs to the high-frequency BL Lac (HBL) class, as its synchrotron spectral component peaks in the x-ray regime. The x-ray spectrum around the synchrotron peak exhibits significant curvature that has been interpreted in terms of a log-parabola function. X-ray spectral analysis of Mkn 421 using *NuSTAR* (3–79 keV) observations, reveals that during the low-flux state of the source in January 2013, the hard x-ray spectra were well represented by a steep power-law model with a photon index saturating at ~ 3 [41,42]. However, the observed x-ray spectrum also shows a significant curvature during high-flux states in April 2013 [22]. This curvature persists even in the hard x-rays, which makes it (in spite of the fact that some blending of components cannot be excluded) challenging to attribute this solely to the spectral transition occurring at the peak of the synchrotron component [43,44]. To explore this further, we have performed a detailed spectral study on the x-ray data of the source. We are particularly interested to understand whether the observed x-ray spectral characteristics allow some inferences on the turbulence properties in the jet. The paper is organized as follows: In Sec. II, we discuss the observation and data reduction procedure, while the x-ray spectral study is described in Sec. III. The summary is presented in Sec. IV.

II. OBSERVATION AND DATA ANALYSIS

Mkn 421 has been observed by *NuSTAR* and *Swift*–*XRT* in both flaring as well as quiescent flux states. For the current study we have selected all the available simultaneous *Swift*–*XRT* and *NuSTAR* observations till 2018 (details are given in Table I). This allows us to analyse the source over a wide range of x-ray energies, from 0.3 to 79 keV. The strategies for analysing these observations are detailed below.

TABLE I. Details of simultaneous *Swift*-XRT and *NuSTAR* observations.

<i>Swift</i> -XRT Obs.ID	Date & time	Exposure (s)	<i>NuSTAR</i> Obs.ID	Date & time	Exposure (s)
35014034	2013-01-15 02:09:59	3958.859	60002023006	2013-01-15 00:56:07	24181
80050003	2013-02-06 01:20:59	9506.827	60002023010	2013-02-06 00:16:07	19302
80050006	2013-02-17 00:03:59	9201.642	60002023014	2013-02-16 23:36:07	17356
80050007	2013-03-04 23:34:25	984.609	60002023016	2013-03-04 23:06:07	17251
80050011	2013-03-11 23:58:59	8425.937	60002023018	2013-03-11 23:01:07	17472
80050013	2013-03-17 01:22:59	8880.74	60002023020	2013-03-17 00:11:07	16554
80050014	2013-04-02 21:01:59	1644.569	60002023022	2013-04-02 17:16:07	24767
80050016	2013-04-11 00:30:59	1118.631	60002023024	2013-04-10 21:26:07	5757
80050019	2013-04-12 21:53:58	9546.279	60002023027	2013-04-12 20:36:07	7629
32792002	2013-04-14 00:38:59	6327.071	60002023029	2013-04-13 21:36:07	16508
35014062	2013-04-15 23:07:59	534.621	60002023033	2013-04-15 22:01:07	17276
35014065	2013-04-17 00:46:59	8842.132	60002023035	2013-04-16 22:21:07	20278
35014066	2013-04-18 00:49:59	6887.219	60002023037	2013-04-18 00:16:07	17795
35014067	2013-04-19 00:52:59	6132.768	60002023039	2013-04-19 00:31:07	15958
34228110	2017-01-04 00:06:57	6021.027	60202048002	2017-01-03 23:51:09	23691
81926001	2017-01-31 23:27:57	1009.619	60202048004	2017-01-31 23:46:09	21564
34228145	2017-02-28 22:46:56	44.62	60202048006	2017-02-28 22:11:09	23906

A. NuSTAR

NuSTAR [45] is a space-based hard x-ray telescope which operates from 3 to 79 keV energy band with an angular resolution of subarcmin. All observations are carried out with two co-aligned, independent telescopes called Focal Plane Module A (FPMA) and B (FPMB). The *NuSTAR* observations were taken from the HEASARC interface by NASA and the data were processed with NuSTARDAS package (Version 2.1.1) available within HEASoft (Version 6.29). The source spectrum is extracted from a circular region with a radius of 50 arcsec centered on the source, while the background is estimated from a circular region with a radius of 70 arcsec that is free of source contamination but near it. The *nuproducts* (Version 0.3.3) was used to obtain source and background spectra after running *nupipeline* (Version 0.4.9) on each observation. The FPMA and FPMB source spectra were then individually grouped to 30 photons per bin using the tool GRPPHA to ensure improved χ^2 statistics.

B. Swift-XRT

The XRT is a focusing x-ray telescope operating in the 0.3–10 keV energy range with an angular resolution of 18 arcsec [46]. The *Swift*-XRT observations were also retrieved from HEASARC interface and the data processed using the XRTDAS software package (Version 3.6.1) available within HEASOFT. We used the observations performed in Windowed Timing (WT) mode and the events with 0–2 grades have been considered in the analysis. The event files were cleaned and calibrated using standard procedures with the *xrtpipeline* (Version 0.13.6) task. A circular region of 30 pixel radius centred at the source was used to extract the source spectrum, and a circular region of

same size devoid of source contamination was used to extract the background spectrum. An annular region with inner and outer radii of 2 and 30 pixels, respectively, was used as source and background regions for the observation with pileup (Obs.ID 80050019). *xrtproducts* (Version v0.4.2) was used to generate the final spectrum. The *xrtmkarf* (Version 0.6.3) task was employed to generate the auxiliary response files (ARFs), and the response matrix files (RMFs) from the *Swift* CALDB were used. The source spectra were then grouped using the GRPPHA tool to ensure a minimum of 20 counts/bin.

III. X-RAY SPECTRAL ANALYSIS AND RESULTS

A. NuSTAR (3–79 keV) regime

To investigate the curvature in the hard x-ray regime, we fitted the *NuSTAR* observations (3–79 keV) of the source, using three models available in XSPEC namely, power-law (PL), log-parabola (LP), and a power-law with an exponential cutoff (CPL). These models are defined as

$$F(\epsilon) \propto \epsilon^{-\Gamma} \quad (\text{PL}), \quad (1)$$

where ϵ is the photon energy, and Γ represents the power-law index

$$F(\epsilon) \propto \left(\frac{\epsilon}{\epsilon_0}\right)^{-\alpha-\beta \log(\epsilon/\epsilon_0)} \quad (\text{LP}), \quad (2)$$

where α is the spectral slope at energy ϵ_0 , and β is the spectral curvature, and

$$F(\epsilon) \propto \epsilon^{-p} \exp[-(\epsilon/\epsilon_c)] \quad (\text{CPL}), \quad (3)$$

TABLE II. Fit parameters of *NuSTAR* (3–79 keV) spectra as modeled with PL, LP and CPL.

<i>NuSTAR</i> Obs.ID	Flux (3–79 keV)	PL		LP($\epsilon_0=5$ keV)			CPL		
		Γ	χ^2_{red}	α	β	χ^2_{red}	p	ϵ_c (keV)	χ^2_{red}
60002023006	-9.954 ± 0.004	3.03 ± 0.01	1.05 (563)	2.95 ± 0.02	0.31 ± 0.06	0.92 (562)	2.82 ± 0.05	$35.12^{+9.75}_{-6.47}$	0.94 (562)
60002023010	-9.842 ± 0.004	2.95 ± 0.01	1.32 (570)	2.83 ± 0.02	0.41 ± 0.06	1.04 (569)	2.64 ± 0.05	$24.99^{+4.49}_{-3.41}$	1.06 (569)
60002023014	-10.187 ± 0.007	3.02 ± 0.02	1.06 (419)	3 ± 0.03	0.11 ± 0.09	1.05 (418)
60002023016	-9.779 ± 0.004	3.01 ± 0.01	1.11 (557)	2.95 ± 0.02	0.25 ± 0.06	1.01 (556)	2.85 ± 0.05	$44.97^{+16.44}_{-9.8}$	1.03 (556)
60002023018	-9.906 ± 0.005	3.09 ± 0.02	1.04 (509)	3.04 ± 0.02	0.2 ± 0.07	0.99 (508)	2.96 ± 0.05	$53.64^{+31.18}_{-14.91}$	1 (508)
60002023020	-9.731 ± 0.005	2.77 ± 0.01	1.18 (595)	2.68 ± 0.02	0.28 ± 0.05	1.04 (594)	2.58 ± 0.04	$40.77^{+10.57}_{-7.19}$	1.06 (594)
60002023022	-9.343 ± 0.002	2.74 ± 0.01	1.51 (898)	2.64 ± 0.01	0.3 ± 0.03	1.03 (897)	2.52 ± 0.02	$38.28^{+3.89}_{-3.29}$	1.06 (897)
60002023024	-9.201 ± 0.003	2.9 ± 0.01	1.47 (620)	2.78 ± 0.02	0.39 ± 0.05	1.11 (619)	2.61 ± 0.04	$27.88^{+4.2}_{-3.33}$	1.14 (619)
60002023027	-8.624 ± 0.002	2.62 ± 0.01	2.63 (1023)	2.45 ± 0.01	0.44 ± 0.02	0.94 (1022)	2.29 ± 0.02	$26.4^{+1.36}_{-1.26}$	1.01 (1022)
60002023029	-9.085 ± 0.002	2.79 ± 0.01	2.06 (917)	2.65 ± 0.01	0.42 ± 0.02	0.98 (916)	2.48 ± 0.02	$26.67^{+1.83}_{-1.64}$	1.08 (916)
60002023033	-9.014 ± 0.002	2.59 ± 0.01	1.86 (1019)	2.46 ± 0.01	0.33 ± 0.02	1.01 (1018)	2.34 ± 0.02	$35.89^{+2.5}_{-2.23}$	1.02 (1018)
60002023035	-8.934 ± 0.002	2.39 ± 0.01	2.33 (1182)	2.25 ± 0.01	0.35 ± 0.02	1.07 (1181)	2.13 ± 0.01	$35.77^{+1.9}_{-1.74}$	1.1 (1181)
60002023037	-9.835 ± 0.004	2.85 ± 0.01	1.31 (568)	2.72 ± 0.02	0.4 ± 0.06	1.05 (567)	2.55 ± 0.05	$26.61^{+4.85}_{-3.67}$	1.05 (567)
60002023039	-9.868 ± 0.005	2.94 ± 0.02	0.98 (519)	2.88 ± 0.02	0.22 ± 0.06	0.91 (518)	2.79 ± 0.05	$50.09^{+23.58}_{-12.58}$	0.92 (518)
60202048002	-9.269 ± 0.003	2.45 ± 0.01	1.39 (1006)	2.36 ± 0.01	0.22 ± 0.02	1.1 (1005)	2.29 ± 0.02	$60.22^{+7.58}_{-6.17}$	1.14 (1005)
60202048004	-9.247 ± 0.003	2.45 ± 0.01	1.72 (1001)	2.31 ± 0.01	0.33 ± 0.02	1.04 (1000)	2.2 ± 0.02	$37.22^{+2.94}_{-2.59}$	1.06 (1000)
60202048006	-9.261 ± 0.002	2.49 ± 0.01	1.75 (996)	2.37 ± 0.01	0.31 ± 0.02	1.13 (995)	2.26 ± 0.02	$39.53^{+3.31}_{-2.89}$	1.16 (995)

where p represents the power-law index, and ϵ_c characterizes the position of the cutoff energy. The spectral peak ($\epsilon^2 F(\epsilon)$ representation) of the log-parabola function is obtained from

$$\epsilon_p = \epsilon_0 10^{\frac{2-\alpha}{2\beta}}. \quad (4)$$

The neutral hydrogen column density, inclusive of both HI and HII was fixed at $N_H = 2.03 \times 10^{20} \text{ cm}^{-2}$

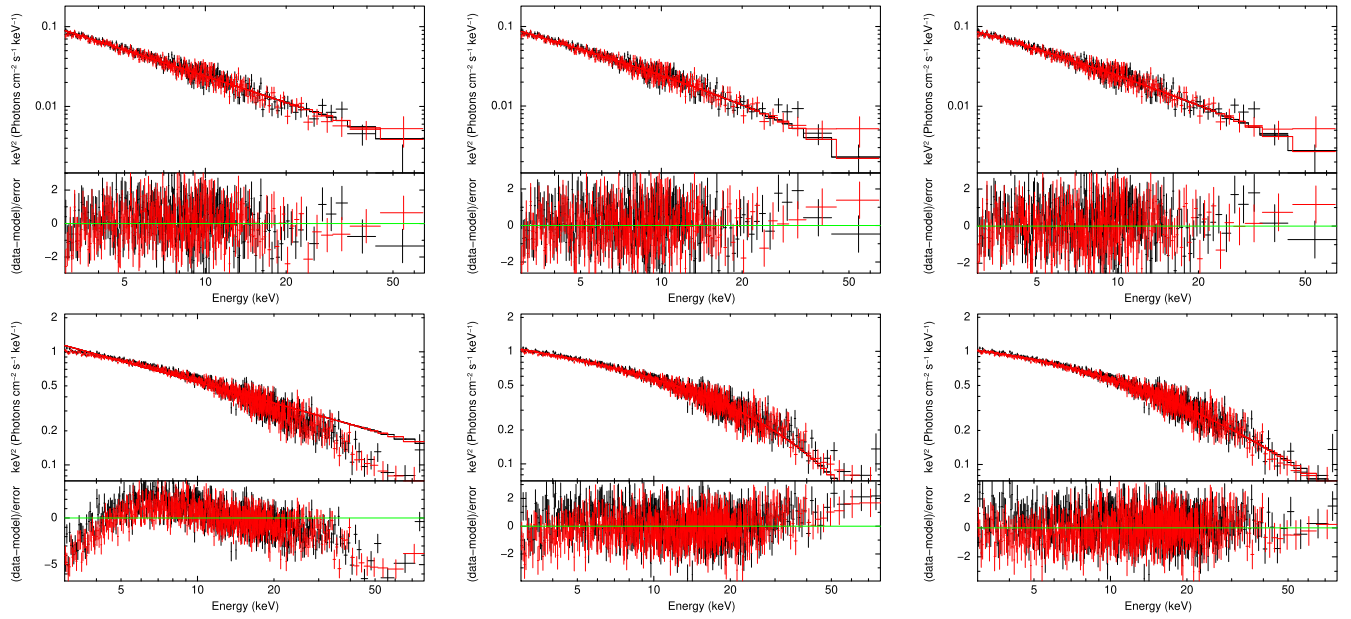


FIG. 1. Spectral fits (*NuSTAR* alone) using the PL, CPL and LP model (left to right) for the ObsIDs 60002023018 (low-flux state) and 60002023027 (high-flux state) are shown in the upper and lower panels, respectively. Significant curvature is apparent in the high flux state.

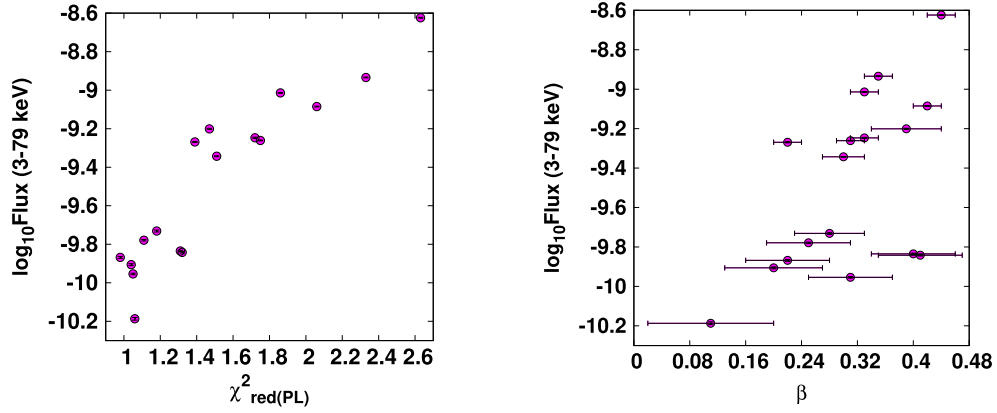


FIG. 2. Scatter plots (*NuSTAR* alone) showing flux, along with reduced chi-square values for the PL fit (left), and LP curvature values β (right).

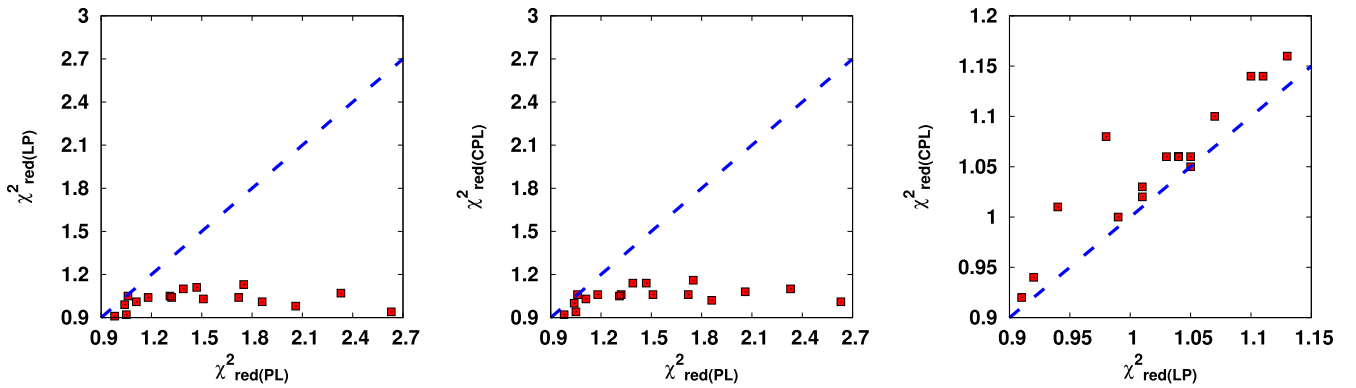


FIG. 3. Scatter plots between the reduced chi-square values of *NuSTAR* data fitted with the models PL, LP and CPL along with the identity line.

throughout the analysis. The best-fit parameters of these models are presented in Table II. We observe that most of the low-flux states are well fitted with a steep power-law model, yielding a photon index saturating at ~ 3 , as reported

earlier [42]. In contrast, the high-flux states exhibit significant curvature and deviate from a simple power-law model (see Fig. 1). The spectral fittings using the PL, LP, and CPL models for a sample of low and high flux states

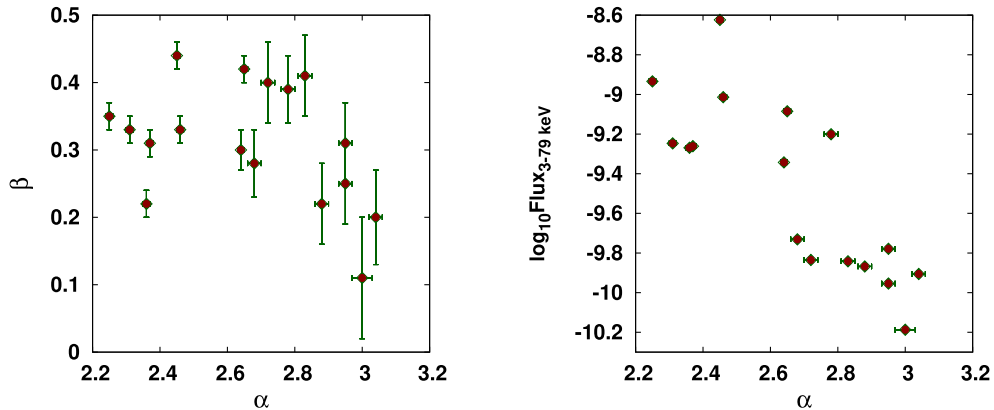


FIG. 4. Scatter plots (*NuSTAR* alone) showing LP index α , along with spectral curvature β (left), and flux in the 3–79 keV range (right).

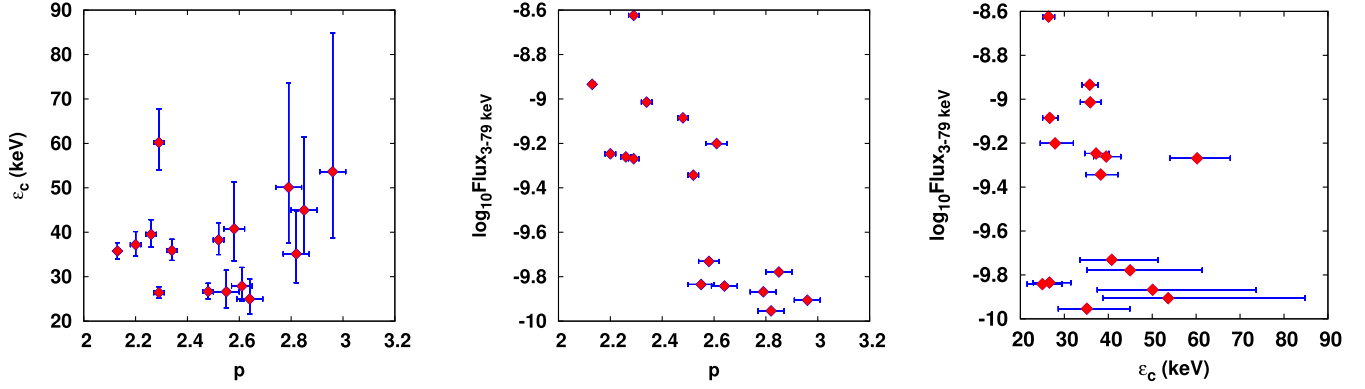


FIG. 5. Scatter plots (*NuSTAR* alone) showing best-fit CPL model parameters: index and cutoff energy (in keV), index and flux, and cutoff energy and flux (from left to right).

are shown in Fig. 1. Figure 2 illustrates the change in the reduced chi-square value of the PL fit (left) and the spectral curvature (right) as the flux increases.

Our analysis provides strong evidence for spectral curvature in the *NuSTAR* regime, with a LP/CPL model clearly preferred over a pure PL model in high flux states. The plots between reduced chi-square values for the spectral fittings with the PL, LP, and CPL models [$\chi_{\text{red}}^2(\text{PL})$, $\chi_{\text{red}}^2(\text{LP})$, and $\chi_{\text{red}}^2(\text{CPL})$] are shown in Fig. 3. Scatter plots showing the best-fit LP and CPL model parameters, and with the flux, are depicted in Figs. 4 and 5, respectively. To identify the dependence between these best-fit parameters, we performed a Spearman rank correlation analysis between various quantities obtained from the spectral fit. The Spearman rank correlation study

between the LP model parameters α and β yields a correlation coefficient, $r_s = -0.41$ with a null hypothesis probability, $p = 0.104$. This result is consistent with previous studies which reported that no significant correlation was observed [22,33]. However, an anticorrelation is witnessed between α and the flux ($r_s = -0.81$, $p < 0.001$), indicating that the spectra get harder during brighter states of the source. This harder when brighter behavior of the source has already been reported earlier [18,22,29,31,32]. The spectral fittings with the simple CPL model allows to constrain well the cutoff energy during high-flux states. Here no correlation is observed between p and ϵ_c ($r_s = 0.16$, $p = 0.556$), while a significant anticorrelation between p and flux ($r_s = -0.79$, $p < 0.001$) is seen.

TABLE III. The best-fit parameters of combined *Swift*-XRT and *NuSTAR* spectral fitting with a LP and a simple CPL model, respectively.

Obs.ID		Flux (0.3–79 keV)	LP ($\epsilon_0 = 5$ keV)				CPL		
<i>Swift</i> -XRT	<i>NuSTAR</i>		α	β	ϵ_p (keV)	χ_{red}^2 (dof)	p	ϵ_c (keV)	χ_{red}^2 (dof)
35014034	60002023006	-9.696 ± 0.003	2.93 ± 0.01	0.34 ± 0.01	0.22 ± 0.02	0.97 (962)	2.38 ± 0.01	11.5 ± 0.42	1.17 (962)
80050003	60002023010	-9.602 ± 0.003	2.81 ± 0.01	0.36 ± 0.01	0.37 ± 0.02	1.27 (1110)	2.23 ± 0.01	10.37 ± 0.3	1.4 (1110)
80050006	60002023014	-9.93 ± 0.004	2.94 ± 0.02	0.25 ± 0.01	0.07 ± 0.01	1.19 (848)	2.51 ± 0.01	14.4 ± 0.87	1.3 (848)
80050007	60002023016	-9.523 ± 0.003	2.92 ± 0.01	0.32 ± 0.02	0.19 ± 0.03	1.1 (822)	2.46 ± 0.02	13.71 ± 0.72	1.34 (822)
80050011	60002023018	-9.639 ± 0.003	2.98 ± 0.01	0.34 ± 0.01	0.17 ± 0.01	1.1 (1001)	2.42 ± 0.01	10.73 ± 0.38	1.35 (1001)
80050013	60002023020	-9.521 ± 0.003	2.67 ± 0.01	0.24 ± 0.01	0.19 ± 0.02	1.16 (1126)	2.29 ± 0.01	16.97 ± 0.69	1.2 (1126)
80050014	60002023022	-9.146 ± 0.002	2.64 ± 0.01	0.31 ± 0.01	0.47 ± 0.03	1.06 (1338)	2.23 ± 0.01	16.45 ± 0.46	1.62 (1338)
80050016	60002023024	-8.972 ± 0.002	2.78 ± 0.01	0.36 ± 0.01	0.41 ± 0.02	1.18 (1039)	2.23 ± 0.01	11.93 ± 0.38	1.41 (1039)
80050019	60002023027	-8.46 ± 0.001	2.45 ± 0.01	0.43 ± 0.01	1.5 ± 0.03	1.07 (1575)	1.91 ± 1.91	12.16 ± 12.16	2.11 (1575)
32792002	60002023029	-8.874 ± 0.001	2.68 ± 0.01	0.34 ± 0.01	0.51 ± 0.02	1.1 (1411)	2.21 ± 0.01	14.15 ± 0.31	1.52 (1411)
35014062	60002023033	-8.847 ± 0.002	2.47 ± 0.01	0.29 ± 0.01	0.79 ± 0.05	1.07 (1391)	2.19 ± 0.01	22.72 ± 0.83	1.33 (1391)
35014065	60002023035	-8.799 ± 0.001	2.27 ± 0.01	0.28 ± 0.01	1.61 ± 0.05	1.17 (1741)	1.96 ± 0.01	21.77 ± 0.52	1.45 (1741)
35014066	60002023037	-9.6 ± 0.003	2.76 ± 0.01	0.22 ± 0.01	0.1 ± 0.01	1.19 (1068)	2.39 ± 0.01	17.67 ± 0.77	1.14 (1068)
35014067	60002023039	-9.625 ± 0.003	2.85 ± 0.01	0.26 ± 0.01	0.11 ± 0.01	1.05 (1001)	2.43 ± 0.01	14.71 ± 0.65	1.21 (1001)
34228110	60202048002	-9.133 ± 0.002	2.34 ± 0.01	0.26 ± 0.01	1.14 ± 0.08	1.09 (1348)	2.12 ± 0.01	28.88 ± 1.44	1.5 (1348)
81926001	60202048004	-9.105 ± 0.002	2.33 ± 0.01	0.29 ± 0.01	1.33 ± 0.08	1.07 (1385)	2.05 ± 0.01	23.45 ± 0.92	1.29 (1385)
34228145	60202048006	-9.116 ± 0.003	2.37 ± 0.01	0.31 ± 0.02	1.29 ± 0.15	1.11 (1044)	2.25 ± 0.02	37.69 ± 2.64	1.18 (1044)

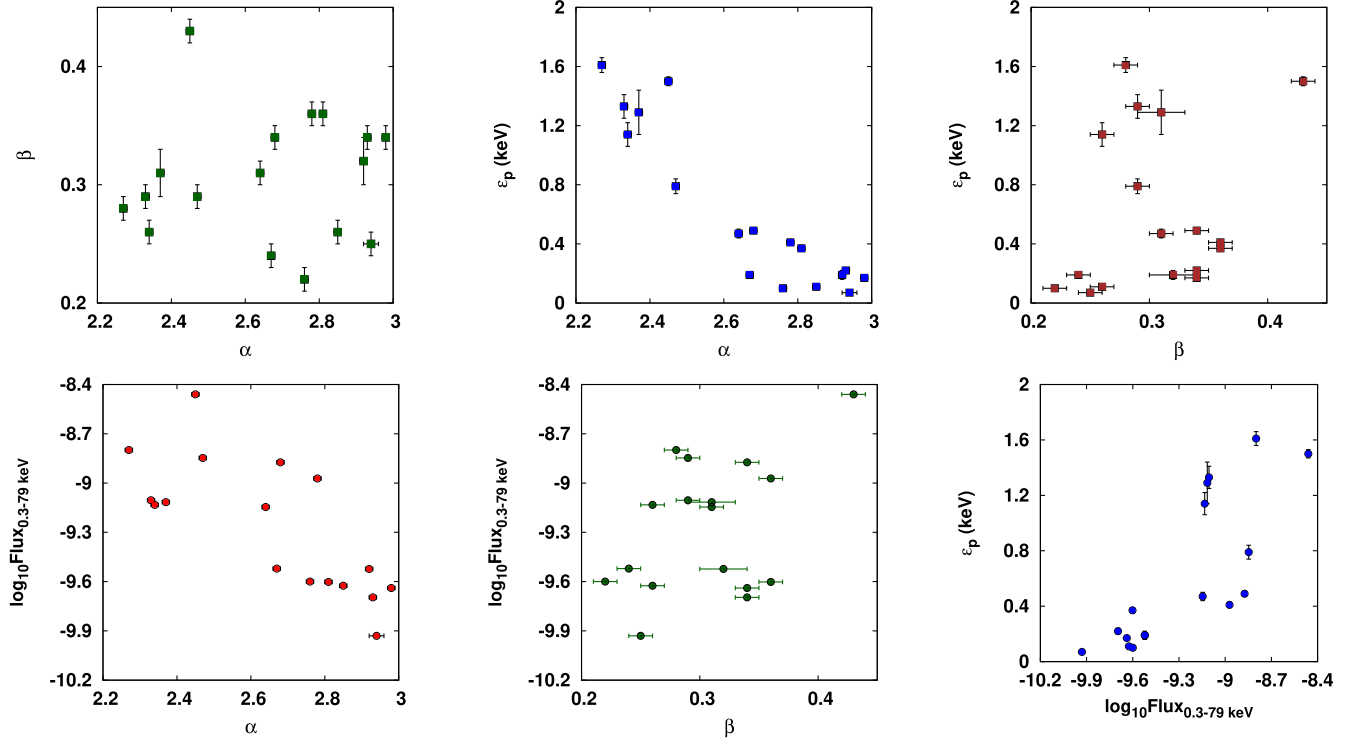


FIG. 6. Scatter plots between the parameters obtained from LP fitting of combined *Swift*-XRT and *NuSTAR* data. The upper panel represents plots between index (α) and curvature (β), α and peak energy (ϵ_p), and β and ϵ_p (from left to right). The lower panel shows the variation of flux in 0.3 to 79 keV with α , β and ϵ_p , respectively (from left to right).

B. Combined *NuSTAR* and *Swift*-XRT (0.3–79 keV) regime

In order to gain further insights, we have also studied the broad x-ray spectra of Mkn 421 ranging from 0.3 to 79 keV using simultaneous *Swift*-XRT and *NuSTAR* observations, employing the log-parabola (LP) and simple exponential cutoff (CPL) model, respectively. These x-ray spectra exhibits significant curvature, and a LP model generally provides a better fit when compared to a simple CPL model. The best-fit parameters are presented in Table III, and the scatter plots between LP parameters and the flux are shown in Fig. 6. Again, we observe no correlation between the α and β ($r_s = 0.17$, $p = 0.521$). Additionally, there was no significant correlation between β and peak energy, ϵ_p , ($r_s = 0.31$, $p = 0.227$), whereas α showed a strong negative correlation with ϵ_p ($r_s = -0.86$, $p < 0.001$). Furthermore, we noted a strong negative correlation between α and flux ($r_s = -0.80$, $p < 0.001$), and ϵ_p being significantly correlated with flux ($r_s = 0.85$, $p < 0.001$). These correlations suggest that during flares, the spectral index hardens and the spectral peak moves toward higher energies.

The absence of a significant correlation among the LP parameters, even in the broad energy range studied here, indicates that the changes in spectral characteristics cannot simply be ascribed to the energy-dependence of the particle

acceleration process as proposed in ref. [18]. Additionally, such a model is unable to account for the broadband SED of blazars [18,21,22]. Hence, an alternate physically motivated choice could be a CPL type model. On the other hand, the foregoing analysis indicates that a simple (purely exponential) CPL model does not provide a better fit to the broad x-ray spectra of the source, particularly in high flux states. To explore this further, we next study the broadband x-ray spectrum using a power-law with a modified exponential cutoff, as might be expected to occur in shock-type acceleration scenarios (see Sec. I).

C. Probing a power-law with modified exponential cutoff

In the context of shock acceleration scenarios, the electron distribution exhibits a simple exponential cutoff form only when diffusion is independent of energy. The shape of the particle distribution deviates from this as the diffusion coefficient becomes energy-dependent, leading to a corresponding change in the synchrotron cutoff (i.e., typically subexponential) shape [39,40]. In HBL sources such as Mkn 421, the maximum achievable electron energies are limited by synchrotron losses. The spectral index evolution around the synchrotron (SED) peak does not support a simple cooling break origin of the peak frequency, rather might be affected by the blending of

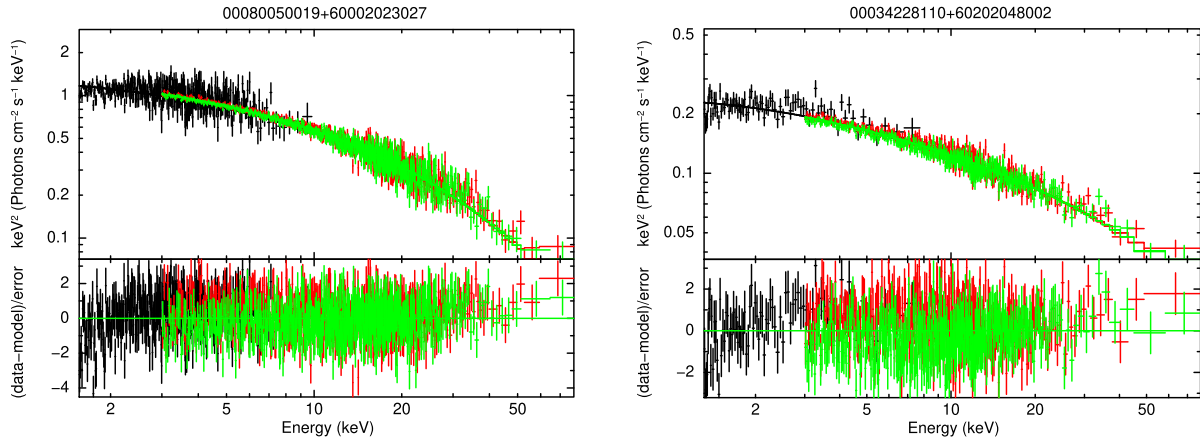


FIG. 7. Spectral fit from ϵ_p -79 keV using the MCPL model for the obsID 00080050019 + 60002023027 (left) and 00034228110 + 60202048002 (right).

different components [e.g., 16]. At hard x-rays, where the synchrotron spectrum declines, we may expect the emission to be more dominated by a single component, particularly during higher flux states. Additionally, the high-energy end of the spectrum is likely to be populated by a cooled electron distribution. To explore the spectral curvature toward high energies in more detail, we thus

perform spectral fits to the x-ray data above the synchrotron SED peak (with $\epsilon_p > 0.3$ keV) using a modified CPL (MCPL) model

$$F(\epsilon) \propto \epsilon^{-p} \exp[-(\epsilon/\epsilon_c)^\zeta] \quad (\text{MCPL}), \quad (5)$$

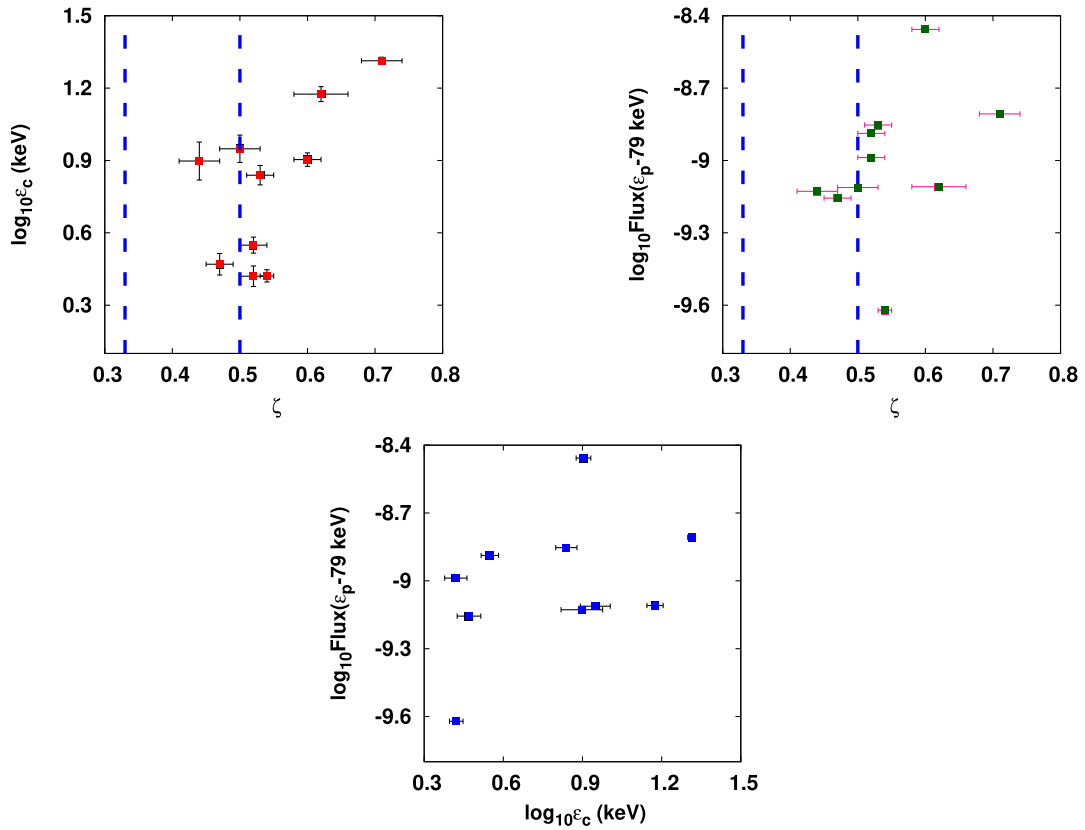


FIG. 8. Scatter plots between best-fit parameters for the MCPL model (ϵ_p -79 keV). The upper left panel is for ζ and cutoff energy (ϵ_c), right is for ζ and flux in ϵ_p -79 keV, and the lower panel is for ϵ_c and flux in ϵ_p -79 keV. The dotted vertical lines represent ζ corresponding to hard-sphere (0.33) and Bohm (0.5).

TABLE IV. Best fit parameters using the MCPL model (cooled $p = 2$) for the energy range ϵ_p -79 keV.

Obs.ID		ϵ_p (keV)	ϵ_c (keV)	ζ	$\chi^2_{\text{red}}(\text{dof})$	Flux (ϵ_p -79 keV)
<i>Swift</i> -XRT	<i>NuSTAR</i>					
80050003	60002023010	0.37 ± 0.02	2.64 ± 0.16	0.54 ± 0.01	1.2 (1106)	-9.621 ± 0.003
80050014	60002023022	0.47 ± 0.03	2.95 ± 0.32	0.47 ± 0.02	1.17 (1323)	-9.156 ± 0.002
80050016	60002023024	0.41 ± 0.02	2.63 ± 0.27	0.52 ± 0.02	1.18 (1030)	-8.988 ± 0.003
80050019	60002023027	1.5 ± 0.03	8.01 ± 0.53	0.6 ± 0.02	1.03 (1458)	-8.457 ± 0.002
32792002	60002023029	0.49 ± 0.02	3.54 ± 0.28	0.52 ± 0.02	1.1 (1394)	-8.888 ± 0.002
35014062	60002023033	0.79 ± 0.05	6.9 ± 0.66	0.53 ± 0.02	1.09 (1345)	-8.853 ± 0.002
35014065	60002023035	1.61 ± 0.05	20.58 ± 0.66	0.71 ± 0.03	1.05 (1613)	-8.807 ± 0.002
34228110	60202048002	1.14 ± 0.08	7.9 ± 1.54	0.44 ± 0.04	1.11 (1266)	-9.128 ± 0.003
81926001	60202048004	1.33 ± 0.08	14.96 ± 1.01	0.62 ± 0.04	1.06 (1285)	-9.109 ± 0.003
34228145	60202048006	1.29 ± 0.15	8.88 ± 1.18	0.5 ± 0.03	1.12 (1015)	-9.112 ± 0.003

where p represents the power-law index, ϵ_c characterizes the position of the cutoff energy, and the parameter ζ governs the steepness of the cutoff. This function is added as a local model in XSPEC, and we perform spectral fitting for the combined simultaneous *Swift*-XRT and *NuSTAR* observations from ϵ_p to 79 keV.

Among the total 17 simultaneous *Swift*-XRT and *NuSTAR* observations we found only for 10 epochs, the peak falls in between 0.3–79 keV. Most of these epochs are during high-flux states (except obsID. 80050003+60002023010), and all these epochs are considered for the MCPL fit. The considered x-ray spectra did not allow us to constrain all parameters of the model. Hence, we performed a fitting with p fixed to a value 2, representing a cooled particle distribution. This choice may be appropriate since we are interested in the spectrum above ϵ_p where synchrotron losses dominate. The sample spectral fits of MCPL model are shown in Fig. 7. The modified CPL model represents well the spectrum above ϵ_p and the best-fit parameters ϵ_c and ζ are shown in Table IV. The scatter plots between the fitting parameters, and with the flux are shown in Fig. 8. We performed a Spearman

correlation analysis and did not find a significant correlation between the MCPL model parameters ϵ_c and ζ ($r_s = 0.45$, $p = 0.192$). Also, no significant correlations are observed between ϵ_c and flux ($r_s = 0.42$, $p = 0.229$), and ζ and flux ($r_s = 0.55$, $p = 0.102$).

Constraining the ζ -parameter in the x-ray spectrum can provide insights into the parent particle distribution. In the case of synchrotron emission, the parameter ζ is linked to the primary particle distribution through the relation $\zeta = \frac{\beta_e}{\beta_e + 2}$ [40]. Therefore, the value of ζ is expected to be 0.33 in the case of energy-independent diffusion ($\beta_e = 1$), while Bohm-type diffusion ($\beta_e = 2$) results in $\zeta = 0.5$. As can be seen from Table IV, the inferred ζ -values favor a Bohm-type behavior.

For comparison, we also repeated this analysis by fixing ζ at the values corresponding to hard-sphere and Bohm-type diffusion, which are 0.33 and 0.5, respectively (Table V). The best-fit parameters revealed that $\zeta = 0.5$ leads to an index p closer to ~ 2 , supporting our previous assumption of a cooled distribution above ϵ_p . Therefore, the results appear consistent with a cooled particle

TABLE V. Best fit parameters using the MCPL model by assuming Bohm($\zeta = 0.5$) and Hard-sphere($\zeta = 0.33$) for ϵ_p -79 keV fit.

Obs.ID		Bohm: $\zeta = 0.5$				Hard-sphere: $\zeta = 0.33$		
<i>Swift</i> -XRT	<i>NuSTAR</i>	ϵ_p (keV)	p	ϵ_c	$\chi^2_{\text{red}}(\text{dof})$	p	ϵ_c	$\chi^2_{\text{red}}(\text{dof})$
80050003	60002023010	0.37 ± 0.02	1.95 ± 0.02	1.84 ± 0.1	1.2 (1106)	1.63 ± 0.02	0.11 ± 0.01	1.19 (1106)
80050014	60002023022	0.47 ± 0.03	2 ± 0.02	3.6 ± 0.22	1.18 (1323)	1.72 ± 0.03	0.25 ± 0.02	1.12 (1323)
80050016	60002023024	0.41 ± 0.02	1.97 ± 0.02	2.2 ± 0.14	1.17 (1030)	1.65 ± 0.03	0.13 ± 0.01	1.16 (1030)
80050019	60002023027	1.5 ± 0.03	1.83 ± 0.03	3.33 ± 0.24	1.01 (1457)	1.43 ± 0.04	0.16 ± 0.02	0.98 (1457)
32792002	60002023029	0.49 ± 0.02	1.95 ± 0.02	2.75 ± 0.13	1.1 (1394)	1.64 ± 0.03	0.17 ± 0.01	1.06 (1394)
35014062	60002023033	0.79 ± 0.05	1.93 ± 0.03	4.83 ± 0.41	1.08 (1345)	1.6 ± 0.04	0.3 ± 0.04	1.05 (1345)
35014065	60002023035	1.61 ± 0.05	1.8 ± 0.02	6.27 ± 0.51	1.03 (1613)	1.49 ± 0.04	0.41 ± 0.05	1.03 (1613)
34228110	60202048002	1.14 ± 0.08	2.04 ± 0.03	13.05 ± 1.97	1.11 (1266)	1.82 ± 0.05	1.19 ± 0.25	1.1 (1266)
81926001	60202048004	1.33 ± 0.08	1.86 ± 0.03	6.24 ± 0.7	1.05 (1284)	1.55 ± 0.05	0.4 ± 0.06	1.04 (1284)
34228145	60202048006	1.29 ± 0.15	1.99 ± 0.04	8.32 ± 1.1	1.12 (1015)	1.71 ± 0.06	0.6 ± 0.11	1.12 (1015)

distribution with a cutoff shaped by Bohm-type diffusion ($\beta_e = 2$).

IV. SUMMARY

We have conducted a detailed study of the x-ray spectra of Mkn 421 using simultaneous *Swift*-XRT and *NuSTAR* observations. Most of our observations considered are during high flux states (unlike ref. [42] for example) and enables us to investigate the spectral curvature in the hard x-ray regime more rigorously. Our spectral study of *NuSTAR* observations using power-law (PL), log-parabolic (LP), and simple exponential cutoff power-law (CPL) models suggests that LP and CPL are clearly preferred over a simple PL. This provides strong evidence of spectral curvature in the 3–79 keV energy regime. We also examined the broad (*Swift*-XRT and *NuSTAR*) x-ray spectra, spanning from 0.3 to 79 keV with LP and CPL models, indicating that LP provides a better fit compared to CPL. However, the lack of a significant correlation between the LP parameters suggests that the variations in spectral characteristics cannot be attributed to the energy-dependence of the particle acceleration process.

The curvature in the x-ray spectrum is closely linked to the primary electron distribution. The acceleration of electrons at shocks is a favored mechanism for generating non-thermal particle distributions in astrophysical jets. In the presence of radiative losses like the synchrotron process, the accelerated electron distribution will be a broken power-law with a modified exponential cutoff at the maximum available electron energy. The resultant synchrotron spectrum from such a particle distribution will always be a power-law with a sub-exponential cutoff, and we found that a MCPL function can satisfactorily reproduce the data beyond the SED peak. Further, the results are consistent with a scenario where the hard x-ray spectrum is due to a cooled electron distribution, with the highest energy part shaped by Bohm-type diffusion. For a strong shock that is non-relativistic in the jet frame ($\Gamma_s = \Gamma_j \Gamma_b (1 - \beta_b \beta_j) \sim 1$, with $\Gamma_j \gg 1$ being the jet Lorentz factor and Γ_b the “blob” Lorentz factor), the characteristic acceleration timescale is approximately given by $t'_{\text{acc}} \simeq 10\kappa'/u_s^2$ where $\kappa' = (1/3)\lambda'c$ and

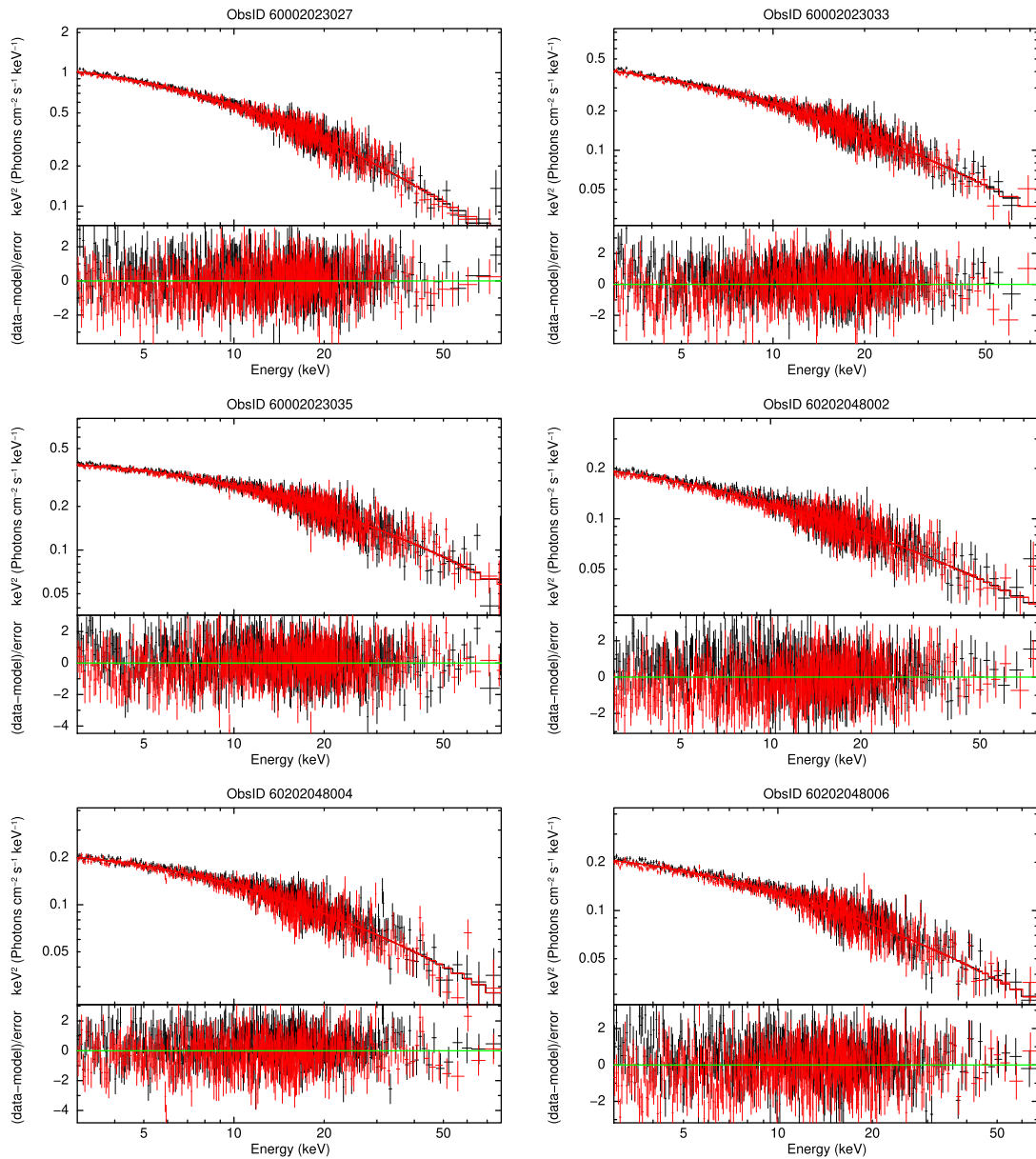
$\lambda' \sim r'_g = \gamma'_e m_e c^2 / (eB')$ in the Bohm limit [e.g., 12]. Balancing acceleration with cooling, $t'_{\text{syn}} = 9m_e^3 c^5 / (4e^4 \gamma'_e B'^2)$, one can estimate maximum achievable electron energies ($\gamma'_{e,m}$). The corresponding synchrotron photon energy $\epsilon'_c \propto \gamma'^2_{e,m} B'$ can be compared to the synchrotron cutoff energies $\epsilon_c \sim 10$ keV inferred from observations (Table IV) taking beaming ($\epsilon_c \sim \Gamma_j \epsilon'_c$) into account. The result then substantiates the initial assumption of non-relativistic shock acceleration.

Though the observed spectral curvature in the hard x-ray supports Bohm-type diffusion during flares in the jet, other possibilities are not yet to be ruled out. For instance, an energy-dependent escape timescale or the superposition of multiple broken power-law components might also contribute to spectral curvature. Since the highest-energy electrons are expected to probe the shock vicinity, x-ray spectral analysis along with dedicated polarization studies [e.g., 37] provides a powerful diagnostics of the underlying flow properties. The signature of an electron distribution shaped by Bohm-type diffusion process could in principle be further probed by modeling the resultant γ -ray emission by inverse Compton scattering [47], though in practice, this may be challenging to achieve with current instrumentation [48]. The type of diffusion process can also have an impact on the temporal behavior of the source. Hence, studying the light curve considering acceleration initiated by different diffusion processes will offer additional insights into the underlying characteristics.

ACKNOWLEDGMENTS

This research has made use of data obtained from NASA’s High Energy Astrophysics Science Archive Research Center(HEASARC), a service of the Goddard Space Flight Center and the Smithsonian Astrophysical Observatory. C.B. wishes to thank CSIR, New Delhi (09/043(0198)/2018-EMR-I) for financial support. C.B. is thankful to UGC-SAP and FIST 2 (SR/FIST/PS1-159/2010) (DST, Government of India) for the research facilities in the Department of Physics, University of Calicut. F.M.R. acknowledges support by a DFG grant under RI 1187/8-1.

APPENDIX: SAMPLE X-RAY SPECTRAL FITS WITH A LOG-PARABOLA MODEL (FIGS. 9, 10)

FIG. 9. *NuSTAR* x-ray spectra (3–79 keV) along with log-parabola model.

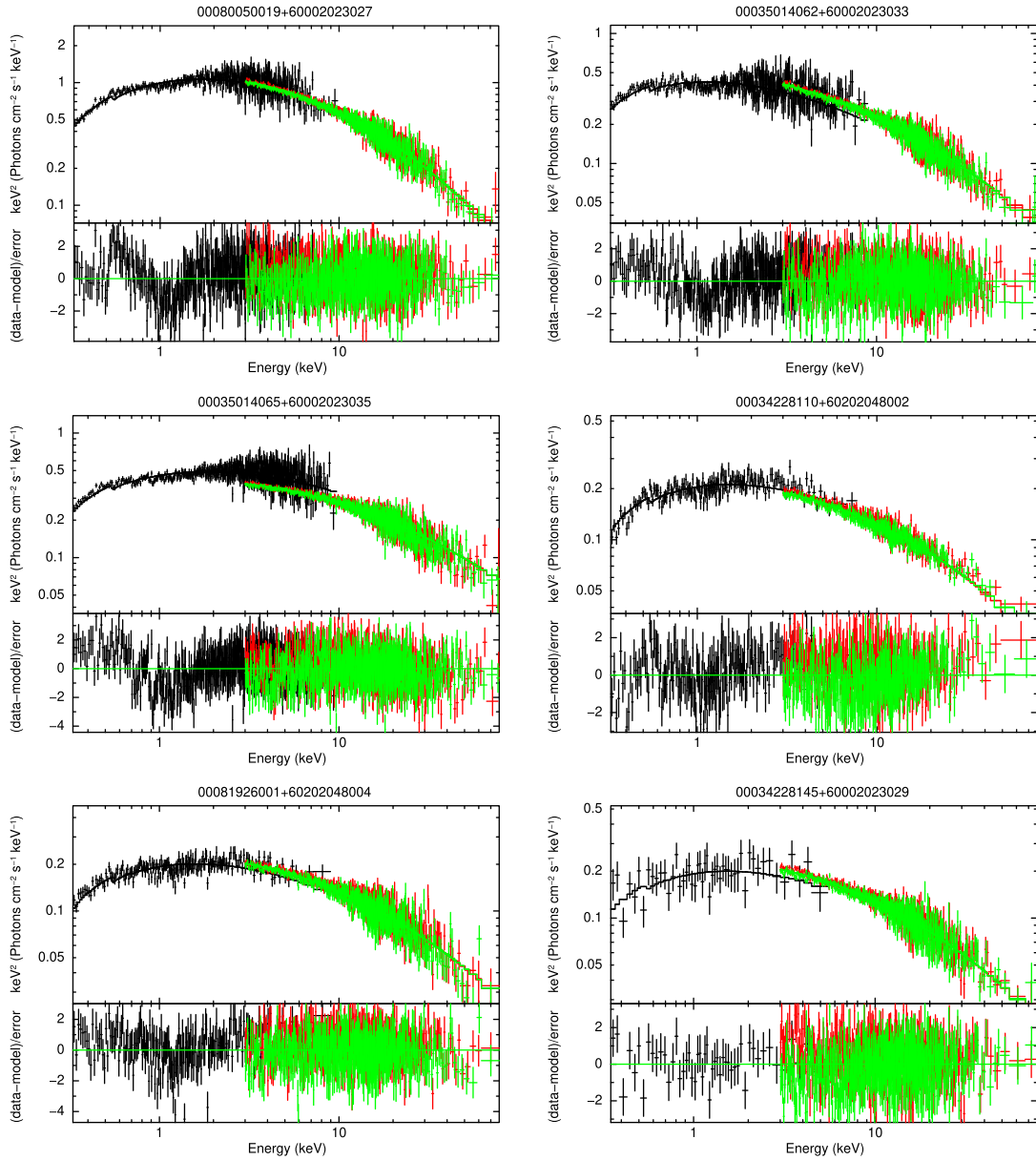


FIG. 10. Combined *Swift*-XRT and *NuSTAR* x-ray spectra (0.3–79 keV) along with log-parabola model.

-
- [1] R. Antonucci, *Annu. Rev. Astron. Astrophys.* **31**, 473 (1993).
 [2] C. M. Urry and P. Padovani, *Publ. Astron. Soc. Pac.* **107**, 803 (1995).
 [3] M.-H. Ulrich, L. Maraschi, and C. M. Urry, *Annu. Rev. Astron. Astrophys.* **35**, 445 (1997).
 [4] G. Ghisellini, I. M. George, and C. Done, *Mon. Not. R. Astron. Soc.* **241**, 43P (1989).
 [5] H. Sol and A. Zech, *Galaxies* **10**, 105 (2022).
 [6] R. M. Sambruna, P. Barr, P. Giommi, L. Maraschi, G. Tagliaferri, and A. Treves, *Astrophys. J. Suppl. Ser.* **95**, 371 (1994).
 [7] F. Tavecchio, L. Maraschi, and G. Ghisellini, *Astrophys. J.* **509**, 608 (1998).
 [8] G. Fossati, A. Celotti, M. Chiaberge, Y.H. Zhang, L. Chiappetti, G. Ghisellini, L. Maraschi, F. Tavecchio, E. Pian, and A. Treves, *Astrophys. J.* **541**, 166 (2000).
 [9] E. Fermi, *Phys. Rev.* **75**, 1169 (1949).

- [10] M. Lemoine, *Phys. Rev. D* **99**, 083006 (2019).
- [11] J. G. Kirk, F. M. Rieger, and A. Mastichiadis, *Astron. Astrophys.* **333**, 452 (1998).
- [12] F. M. Rieger, V. Bosch-Ramon, and P. Duffy, *Astrophys. Space Sci.* **309**, 119 (2007).
- [13] N. S. Kardashev, *Sov. Astron.* **6**, 317 (1962).
- [14] G. B. Rybicki and A. P. Lightman, *Radiative Processes in Astrophysics* (Wiley-VCH, Hoboken, 1986).
- [15] N. Mankuzhiyil, S. Ansoldi, M. Persic, E. Rivers, R. Rothschild, and F. Tavecchio, *Astrophys. J.* **753**, 154 (2012).
- [16] C. Baheejja, S. Sahayanathan, F. M. Rieger, S. K. Jagan, and C. D. Ravikumar, *Mon. Not. R. Astron. Soc.* **514**, 3074 (2022).
- [17] R. Landau, B. Golisch, T. J. Jones, T. W. Jones, J. Pedelty, L. Rudnick, M. L. Sitko, J. Kenney, T. Roellig, E. Salonen, S. Urpo, G. Schmidt, G. Neugebauer, K. Matthews, J. H. Elias, C. Impey, P. Clegg, and S. Harris, *Astrophys. J.* **308**, 78 (1986).
- [18] E. Massaro, M. Perri, P. Giommi, and R. Nesci, *Astron. Astrophys.* **413**, 489 (2004).
- [19] A. Tramacere, P. Giommi, E. Massaro, M. Perri, R. Nesci, S. Colafrancesco, G. Tagliaferri, G. Chincarini, A. Falcone, D. N. Burrows, P. Roming, M. McMath Chester, and N. Gehrels, *Astron. Astrophys.* **467**, 501 (2007).
- [20] L. Chen, *Astrophys. J.* **788**, 179 (2014).
- [21] A. Tramacere, P. Giommi, M. Perri, F. Verrecchia, and G. Tosti, *Astron. Astrophys.* **501**, 879 (2009).
- [22] A. Sinha, A. Shukla, R. Misra, V. R. Chitnis, A. R. Rao, and B. S. Acharya, *Astron. Astrophys.* **580**, A100 (2015).
- [23] S. K. Jagan, S. Sahayanathan, R. Misra, C. D. Ravikumar, and K. Jeena, *Mon. Not. R. Astron. Soc.* **478**, L105 (2018).
- [24] A. Sinha, S. Sahayanathan, B. S. Acharya, G. C. Anupama, V. R. Chitnis, and B. B. Singh, *Astrophys. J.* **836**, 83 (2017).
- [25] J. Bhagwan, A. C. Gupta, I. E. Papadakis, and P. J. Wiita, *Mon. Not. R. Astron. Soc.* **444**, 3647 (2014).
- [26] H. Gaur, L. Chen, R. Misra, S. Sahayanathan, M. F. Gu, P. Kushwaha, and G. C. Dewangan, *Astrophys. J.* **850**, 209 (2017).
- [27] A. Tramacere, E. Massaro, and A. M. Taylor, *Astrophys. J.* **739**, 66 (2011).
- [28] A. Tramacere, F. Massaro, and A. Cavaliere, *Astron. Astrophys.* **466**, 521 (2007).
- [29] F. Massaro, A. Tramacere, A. Cavaliere, M. Perri, and P. Giommi, *Astron. Astrophys.* **478**, 395 (2008).
- [30] B. Kapanadze, S. Vercellone, P. Romano, P. Hughes, M. Aller, H. Aller, O. Kharshiladze, S. Kapanadze, and L. Tabagari, *Astrophys. J.* **854**, 66 (2018).
- [31] B. Kapanadze, S. Vercellone, P. Romano, P. Hughes, M. Aller, H. Aller, O. Kharshiladze, and L. Tabagari, *Astrophys. J.* **858**, 68 (2018).
- [32] B. Kapanadze, A. Gurchumelia, D. Dorner, S. Vercellone, P. Romano, P. Hughes, M. Aller, H. Aller, and O. Kharshiladze, *Astrophys. J. Suppl. Ser.* **247**, 27 (2020).
- [33] P. Goswami, S. Sahayanathan, A. Sinha, R. Misra, and R. Gogoi, *Mon. Not. R. Astron. Soc.* **480**, 2046 (2018).
- [34] P. Goswami, S. Sahayanathan, A. Sinha, and R. Gogoi, *Mon. Not. R. Astron. Soc.* **499**, 2094 (2020).
- [35] A. P. Marscher and W. K. Gear, *Astrophys. J.* **298**, 114 (1985).
- [36] A. Zech and M. Lemoine, *Astron. Astrophys.* **654**, A96 (2021).
- [37] L. Di Gesu *et al.*, *Astrophys. J. Lett.* **938**, L7 (2022).
- [38] L. Di Gesu *et al.*, *Nat. Astron.* **7**, 1245 (2023).
- [39] V. N. Zirakashvili and F. Aharonian, *Astron. Astrophys.* **465**, 695 (2007).
- [40] K. D. Fritz, *Astron. Astrophys.* **214**, 14 (1989).
- [41] J. Kataoka and Ł. Stawarz, *Astrophys. J.* **827**, 55 (2016).
- [42] M. Baloković, *Astrophys. J.* **819**, 156 (2016).
- [43] G. Fossati *et al.*, *Astrophys. J.* **677**, 906 (2008).
- [44] D. Horan *et al.*, *Astrophys. J.* **695**, 596 (2009).
- [45] F. A. Harrison, *Astrophys. J.* **770**, 103 (2013).
- [46] D. N. Burrows, *Space Sci. Rev.* **120**, 165 (2005).
- [47] E. Lefa, S. R. Kelner, and F. A. Aharonian, *Astrophys. J.* **753**, 176 (2012).
- [48] C. Romoli, A. M. Taylor, and F. Aharonian, *Astropart. Phys.* **88**, 38 (2017).